Available online at www.sciencedirect.com

ScienceDirect

Energy Procedia 94 (2016) 290 – 305

Energy Procedia

13th Deep Sea Offshore Wind R&D Conference, EERA DeepWind'2016, 20-22 January 2016, Trondheim, Norway

Parametric Wave Excitation Model for Floating Wind Turbines

Frank Lemmer (né Sandner), Steffen Raach, David Schlipf, Po Wen Cheng

Stuttgart Wind Energy, University of Stuttgart, Allmandring 5B, 70569 Stuttgart, Germany

Abstract

This paper presents a parametric wave disturbance model for an improved representation of the overall system dynamics of a floating wind turbine (FOWT). Hydrodynamic panel codes calculate the frequency-dependent first-order wave excitation force coefficient on rigid floating bodies. This transfer function from wave height to the forces and moments on the body is approximated in this work by a linear time-invariant model. With a causal problem definition the fit to an impulse response shows a good agreement in frequency and time domain for spar-type and semi-submersible-type platforms of floating wind turbines. The disturbance model was coupled to a linear structural FOWT model and the effect of the wave height on the tower-top displacement was compared to the nonlinear model with good agreement. Applications of this parametric model are the inclusion of disturbance dynamics in model-based controller design as well as feedforward control for fatigue load reduction.

Peer-review under responsibility of SINTEF Energi AS

Keywords: Floating wind turbine, wave excitation model, disturbance model, system identification, LTI model, controller design

1. Introduction

Offshore wind turbines increase significantly in size as the development and experience with large plants builds up. The rotors of these turbines make the offshore wind turbine the largest existing rotor-dynamic system. Simplified models, which are the focus of this paper, can be used for conceptual optimization and controller design. Especially linearized models provide the fundamental understanding of the system dynamics through eigenvalue analyses and transfer functions. This knowledge is essential for system and controller design. In general, floating wind turbines (FOWT) are simulated in time domain, taking the structural flexibilities into account. The coupling of the structural deformation with hydrodynamics and aerodynamics stresses the importance of transients, which increases the complexity of linear rigid-body models commonly used in ocean engineering. Cummins equation is the standard approach for the time-domain representation of the first-order radiation and diffraction of a floating body. The wave excitation part of Cummins equation is the focus of this paper. Yu and Falnes [1], developed a state-space model of

* Corresponding author. Tel.: +49 711 685 68332
E-mail address: lemmer@ifb.uni-stuttgart.de

Peer-review under responsibility of SINTEF Energi AS
doi:10.1016/j.egypro.2016.09.186

the wave excitation force of a vertical cylinder in heave direction, aiming at the control of wave energy converters. They analyzed extensively the non-causality of the wave excitation function, or force-RAO, which is due to the fact that the wave forces might arrive at the hull prior to the corresponding free-surface elevation at the location of the floating body.

The objective of this work is to find a parameterized representation of the wave excitation force coefficient, the transfer function from the wave height to the six forces and moments on the floating foundation of a wind turbine, $\boldsymbol{G}_{frc} = \boldsymbol{G}_{\eta \to F}$, see Fig. 1. This means that the wave excitation force time series do not have to be calculated prior to a simulation through an inverse Fourier transform, the wave height is a direct input to the model. Also, this disturbance model is advantageous for the design process of the blade-pitch controller and, furthermore, as an integrated real-time model for model-based control approaches. With wave scanning methods a feedforward control for disturbance attenuation is conceivable, where an incident wave elevation measurement is fed into the LTI model in order to optimize the actuator trajectory for future timesteps. This is comparable to Dynamic Positioning (DP) control, which compensates the motion from second-order hydrodynamic forces. Signal filtering, necessary for an implementation of such a system, is not considered in this work. The methodology in this work follows the model proposed by Yu and Falnes [1]: The solution of the wave excitation function in surge-, heave- and pitch-direction is calculated with a hydrodynamic panel code, see Section 2. The frequency-dependent function is then transformed to time-domain and the resulting impulse response is shifted such that the response in negative times is negligible. This causalized response is then the time-domain data for the system identification. A linear time-invariant (LTI) model is subsequently fitted to the given data with a variable number of poles and zeros in Section 3. The performance of the fitted model can be evaluated with the wave force impulse response directly, but also with the time-domain wave force response to a stochastic wave train. The same wave train can then be used to calculate its corresponding complex energy spectrum, which gives, when multiplied with the wave force transfer function, the wave force response to the same excitation as for the identified model. The method has been applied to two generic floating offshore wind turbine platform geometries, both for the NREL 5 MW reference wind turbine, see [2]. The first is the spar-type shape of the OC3-Hywind model, see [3] with a rather simple cylindrical shape, whereas the second model is the OC4-DeepCwind semi-submersible, see [4]. This one consists of three outer columns with heave-plates at their bottom ends, one central column and braced connectors.

The knowledge of the transfer function from wave height to the system outputs such as rotor speed, tower-top displacement or platform displacements is crucial for the design of controllers using loop-shaping methods. Therefore, the LTI wave excitation model is incorporated in a flexible multibody model for floating wind turbines as shown in Fig. 1, where a general FOWT dynamic system is assembled in terms of linear block diagrams with the identified wave disturbance model. Through a linearization of the nonlinear equations of motion a transfer function from the disturbances like wave height or wind speed to the system states can be obtained. This is shown in Section 4 before summarizing and concluding this work.

2. Time-domain simulation of linear hydrodynamics

As transient load situations are often design-driving for floating wind turbines all relevant standards require various time-domain simulations with wind and wave loads. Therefore, state-of-the-art simulation tools for floating wind turbines are based on a frequency-to-time-domain transformation of the hydrodynamic coefficients. Hydrodynamic panel codes solve a potential flow problem with 3D surface meshes as boundary conditions. Usually the decoupled problems of radiation (or maneuvering) and diffraction (or seakeeping) are considered: The radiation problem is solved for still water with the floating body oscillating at various frequencies. Its linear solution is the 6×6 frequency-dependent radiation damping matrix $\boldsymbol{B}(\omega)$ and the 6×6 frequency-dependent added mass matrix $\boldsymbol{A}(\omega)$. The diffraction problem is solved for a fixed floating body with waves of different frequencies (and directions) as boundary condition. The linear solution of the diffraction problem is the frequency-dependent 6×1 wave excitation force coefficient $\boldsymbol{X}(\omega)$. In frequency-domain the equation of motion can be set up assuming a linear superposition of the radiation and diffraction problem as

$$-\omega^2 \left[\boldsymbol{M} + \boldsymbol{A}(\omega)\right] \tilde{\boldsymbol{\xi}} + j\omega \boldsymbol{B}(\omega) \tilde{\boldsymbol{\xi}} + \boldsymbol{C} \tilde{\boldsymbol{\xi}} = \boldsymbol{X}(\omega) \tilde{\eta}(\omega) \tag{1}$$

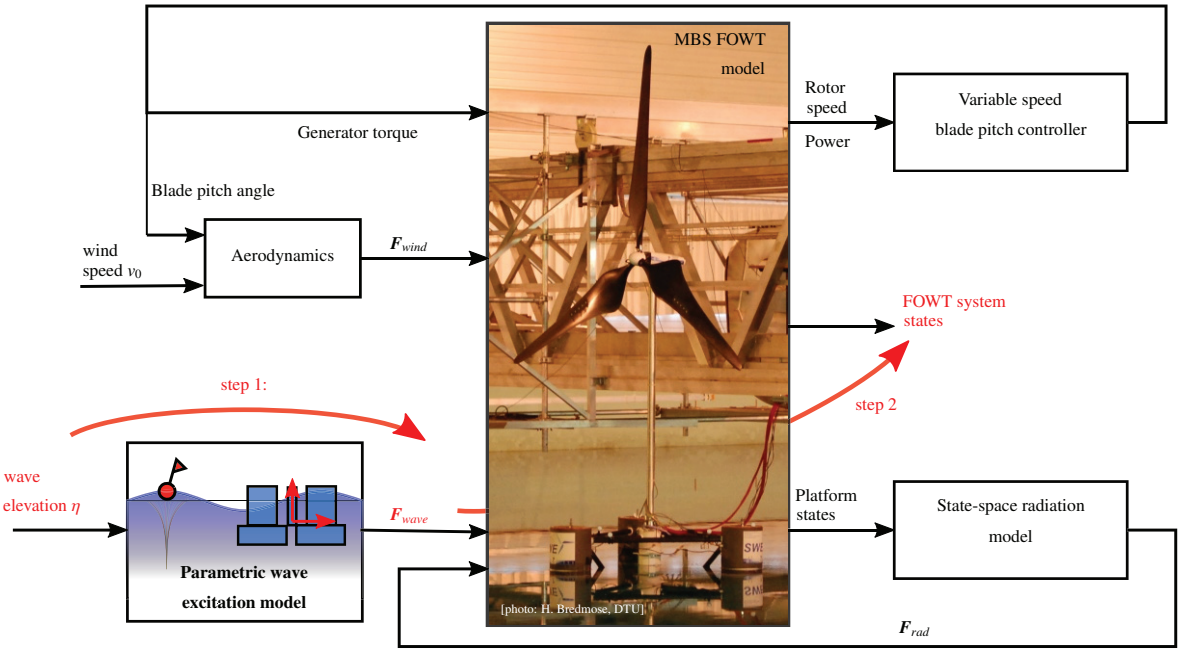

Fig. 1: Coupled FOWT model including dynamic subsystems and disturbance transfer function as block diagram.

with the hydrostatic stiffness $\boldsymbol{C}$ and the 6×1 complex vector of differential generalized coordinates of the unconstrained body in all three directions and orientations $\tilde{\boldsymbol{\xi}}$ and the complex free-surface elevation $\tilde{\eta}(\omega)$, see also [5].

The two potential flow solutions of the coefficients of the left and the right-hand side of eqn. (1) are now specifically useful: The matrices $\boldsymbol{A}(\omega)$ and $\boldsymbol{B}(\omega)$ represent the system properties, whereas $\boldsymbol{X}(\omega)$ represents the excitation force properties of waves on the floating body.

2.1. Frequency-to-time domain transformation

For time-domain simulations of freely floating bodies, Cummins has derived a valid frequency-to-time-domain conversion of eqn. (1). The linear and stationary description in frequency-domain of eqn. (1) needs to be extended to account for transient effects. These transients can be seen as the pressure forces due to radiated waves by a motion impulse of the hull. The frequency-domain dynamics of the fluid particles surrounding the hull are

$$\boldsymbol{K}(j\omega) = \boldsymbol{B}(\omega) + j\omega\,[\boldsymbol{A}(\omega) - \boldsymbol{A}]\,. \tag{2}$$

The "retardation" function $\boldsymbol{K}(j\omega)$ has a real and an imaginary component. While the summand of the damping coefficient is real the one of the added-mass coefficient is imaginary. The time-domain fluid impulse response function $\boldsymbol{K}(j\omega)$ can be obtained according to Ogilvie, [6], by transforming the real part or the imaginary part of eqn. (2) to the time-domain as

$$\boldsymbol{K}(t) = \frac{2}{\pi}\int_0^\infty \boldsymbol{B}(\omega)\cos(\omega t)d\omega = -\frac{2}{\pi}\int_0^\infty \omega\,[\boldsymbol{A}(\omega) - \boldsymbol{A}_\infty]\sin(\omega t)d\omega. \tag{3}$$

Consequently, the retardation function $\boldsymbol{K}(j\omega)$ can be computed from the panel code results and subsequently transformed into time-domain to obtain the impulse response function $\boldsymbol{K}(t)$.

The integral radiation pressure forces can now be written in the time-domain with an acceleration-dependent term with constant coefficient $\boldsymbol{A}$ and the convolution of the impulse response function $\boldsymbol{K}(t)$ with the body velocity $\dot{\boldsymbol{\xi}}$ ac-

cording to Cummins, [7], as

$$\boldsymbol{F}_{rad} = -\boldsymbol{A}\ddot{\boldsymbol{\xi}} - \int_0^t \boldsymbol{K}(t-\tau)\dot{\boldsymbol{\xi}}d\tau. \tag{4}$$

This is commonly implemented in state-of-the-art floating wind simulation tools, like FAST, Bladed and others. Cummins equation is the time-domain equation of motion of a rigid floating body with its center of mass as reference

$$(\boldsymbol{M} + \boldsymbol{A}_\infty)\ddot{\boldsymbol{\xi}} + \int_0^t \boldsymbol{K}(t-\tau)\dot{\boldsymbol{\xi}}(\tau)d\tau + \boldsymbol{C}\boldsymbol{\xi} = \boldsymbol{F}_{wave}. \tag{5}$$

The convolution integral in eqn. (5) brings some computational burden since a time history of platform velocities has to be stored and an integration over a number of past time steps needs to be performed. The number of time steps necessary has to be determined according to the platform model.

In general, the magnitude of the radiation forces on floating wind turbines is not decisive but the effects involved in the radiation problem do alter the dynamics: Although radiation damping contributes only a small portion to the overall damping (which is generally dominated by viscous damping through vortex shedding) the component of the radiation damping force F_{rad} in eqn. (4) which is in phase with the acceleration does change the apparent added mass and inertia at the frequency of oscillation. This is the most significant disadvantage of using the simplified "constant matrix" approach where eqn. (1) is transformed to the time-domain assuming constant coefficients for the added mass and radiation damping $\boldsymbol{A}$ and $\boldsymbol{B}$, respectively as

$$(\boldsymbol{M} + \boldsymbol{A}(\boldsymbol{\omega}_c))\ddot{\boldsymbol{\xi}} + \boldsymbol{B}(\boldsymbol{\omega}_c)\dot{\boldsymbol{\xi}} + \boldsymbol{C}\boldsymbol{\xi} = \boldsymbol{F}_{wave}. \tag{6}$$

Here, the constant frequencies of vector $\boldsymbol{\omega}_c$ can be selected according to the respective eigenfrequencies of the rigid floating body. The linear damping term with the panel code radiation damping coefficient $\boldsymbol{B}(\boldsymbol{\omega}_c)$ can be augmented by damping coefficients from experiments or high-fidelity simulations. Here, the damping coefficients, defined in the definitions of the generic platforms have been used, see Section 4.

The driving force of the right-hand side of eqn. (1) and eqn. (5), the wave excitation force, can be obtained in the frequency-domain by multiplying the force coefficient $\boldsymbol{X}$ with the complex wave spectrum $\tilde{\eta}(\omega)$

$$\boldsymbol{F}_{wave}(\omega) = \boldsymbol{X}\tilde{\eta}(\omega). \tag{7}$$

For conventional time-domain simulations of FOWTs the spectral wave data is a model input. Prior to the simulation the wave force timeseries in all six directions $\boldsymbol{F}_{wave}(t)$ is calculated for the entire simulation time through an inverse Fourier transform

$$\boldsymbol{F}_{wave}(t) = \frac{1}{2\pi}\int_{-\infty}^{\infty} \tilde{\eta}(\omega)\boldsymbol{X}(\omega)e^{j\omega t}d\omega. \tag{8}$$

Note that the wave spectrum $\tilde{\eta}(\omega)$ in eqn. (8) is the amplitude spectrum of the wave height, not the commonly used power spectrum. It is a complex amplitude spectrum with a random phase. This random phase introduces equally random time realizations, see also [8] for a clear derivation.

In summary, frequency-to-time domain conversions can be used directly with the hydrodynamic coefficients calculated by panel codes. The disadvantage is that computationally expensive integrations are necessary either prior to a simulation, in the case of the wave excitation force $\boldsymbol{F}_{wave}$, or during the simulation in the case of the radiation force $\boldsymbol{F}_{rad}$. The next section deals with an alternative description, which represents the wave excitation dynamics through parametric linear time-invariant models.

2.2. Parametric dynamic models

When we talk about a "parametric" model we mean an LTI model with a nonzero number of states in the case of a state-space model or poles, in the case of a linear transfer function. The coefficients of these models (of the characteristic polynomial) are parameterized such that the new LTI model represents the best fit to the original model

from the panel code through methods of system identification. The advantage of these models is mainly that the complete time-domain dynamics are described as a "unified", parametric system without numeric transfer functions

$$\begin{aligned} \dot{\boldsymbol{x}} &= \boldsymbol{A}\boldsymbol{x} + \boldsymbol{B}\boldsymbol{u} \\ \boldsymbol{y} &= \boldsymbol{C}\boldsymbol{x} + \boldsymbol{D}\boldsymbol{u}. \end{aligned} \tag{9}$$

The state vector is denoted by $\boldsymbol{x}$, the input vector by $\boldsymbol{u}$ and the output vector by $\boldsymbol{y}$. On the wave-excitation side this means that the linear wave dynamics from the wave elevation to the forces on the platform are described through a linear dynamic model as explained in the next section. Also for radiation models, the dynamics from the body motion in all six directions to the forces exerted on the moving body itself through the radiated waves. Such LTI models for the radiation problem (representing the convolution integral of eqn. (5)) have been proposed in the literature. See [1], [9] for wave energy converters and [10] and [11] for vessels with the description of the corresponding Matlab toolbox in [12]. The method of fitting a state-space model to a convolution integral has been applied to floating wind turbines and incorporated in NREL's FAST model, [13] in [14]. It is therefore possible to directly compare the performance of coupled time-domain simulations of floating wind turbines using Cummins equation with the fitted LTI radiation model.

Thus, the radiation problem is part of the system matrix $\boldsymbol{A}$, whereas the wave excitation (or diffraction) dynamics is part of the input matrix $\boldsymbol{B}$. Eventually, no integrals appear in the equations of motion and the wave height as "measurable sensor" is a system input instead of the hydrodynamic forces calculated in a pre-processing step. This is especially advantageous for the set up of parametric transfer functions, either of the plant (from system inputs $\boldsymbol{u}$ to outputs $\boldsymbol{y}$, or system states $\boldsymbol{x}$) or from a disturbance (wave height η to outputs or system states). These "disturbance models" are essential for vessel stabilization and disturbance rejection such as DP control, see [15]. Here, a slow feedback control attenuates the excitations from second-order drift forces on offshore supply vessels. For the complex dynamics of floating wind turbines such disturbance rejection methods are very promising, see e.g. [16] for structural control using tuned mass dampers, [17] and [18] for nonlinear and linear model predictive control and [19] for feedforward control. Feedforward control is seen as a very promising application of the wave model of this work since a better system description together with advanced wind and wave sensors can help to reduce fatigue and also extreme loads. Here, first-order wave loads drive the fatigue loads and impact the power fluctuation of FOWTs, which differs from the objectives of DP control. For FOWT feedforward control with the blade pitch angle as controlled variable is conceivable: Using the LTI model of this work for the first-order wave loads one can design a feedforward controller, which reduces the loads or the motion of the floater.

Fitted LTI models of the first-order wave excitation force $\boldsymbol{F}_{wave}$ of eqn. (8) have not been applied yet to floating wind turbines. In the following the method that was applied to a floating vertical cylinder in heave direction by [1] will be applied to two FOWT hulls in surge, heave and pitch-direction.

3. Identification of the wave excitation force

This section deals with the system identification of the frequency-dependent wave excitation force coefficient $\boldsymbol{X}(\omega)$. It is originally calculated by 2D strip-theory or 3D panel codes employing linear potential flow theory. The force vector $\boldsymbol{X}(\omega)$ contains two components: The Froude-Krylov force due to the incident wave pressure on the hull and the force due to diffraction of the wave field. The difficulty of fitting the wave excitation force to an LTI model is the fact that the wave height η used as reference in the panel code for the calculation of $\boldsymbol{X}(\omega)$ is the wave height at the position of the floating body. This results in a "non-causal" transfer function, which means that the forces might arrive at the floating body prior to the wave elevation. In this case the disturbance model input η would no longer be the cause for the output, the wave excitation force. Since potential flow theory shows that ocean waves are dispersive they travel at different phase velocities v_p depending on the wavenumber k or the wavelength λ

$$v_p = \frac{1}{2}\sqrt{\frac{g}{k}} = \frac{1}{2}\sqrt{\frac{g\lambda}{2\pi}}. \tag{10}$$

When selecting a wave height sensor position at some distance from the body against the wave direction the wave excitation force model can be made causal. Falnes has elaborated this problem comprehensively in [20].

System identification can be done based on measurement data of physical experiments, such as model tests, or based on simulation results of a different model. The latter approach is selected here, where we want to avoid the numerically expensive calculation of a convolution integral and identify an LTI model instead. Either time-domain or frequency-domain data can be the basis for system identification, see [21] for a general introduction. Here, an impulse response will be used to fit the parametric model. The next sections will address the causalization of the wave excitation force and the model fit to the impulse response.

3.1. Causalization

In this section the wave excitation problem, or the wave excitation transfer function will be modified to obtain a causal relationship between the wave height η and the six forces on the platform $\boldsymbol{F}_{wave}$. Figure 2 shows the response of the wave excitation force coefficient $\boldsymbol{X}(\omega)$ to a wave height impulse at $t = 0\,\mathrm{s}$ in red. The response has been calculated through an inverse Fast Fourier transform of the wave excitation force coefficient $\boldsymbol{X}(\omega)$. It can be seen that there is a response at negative times, showing the non-causality as described above. A model fit of a non-causal transfer function is not possible and therefore, as discussed above and in [20] a time delay τ_c will be introduced in order to make sure that the transfer function vector $\boldsymbol{G}_{frc}$ is causal for all directions i.

The time delay τ_c is the time by which the causalized impulse response is lagged compared to the original one shown in Fig. 2. This means that the response time of the causalized system is $t_c = t - \tau_c$. Thus, a wave height timeseries at the position of the platform at time t yields its physically corresponding wave force response at the time t_c. In frequency domain the time delay τ_c is converted to a frequency-dependent phase lag $\varphi_c(\omega)$ as

$$\varphi_c(\omega) = \omega\, \tau_c. \tag{11}$$

The time delay τ_c selected for the OC3-Hywind spar in Fig. 2 is $\tau_c = 6\,\mathrm{s}$. It is noted that, due to the dispersion

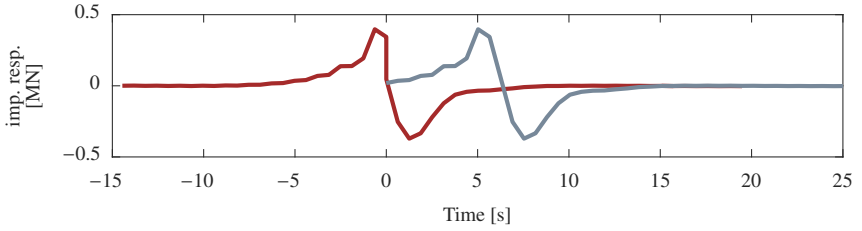

Fig. 2: Non-causal (red) and causalized (grey) wave excitation impulse response of the OC3-spar in surge.

relationship, eqn. (10), the exact position of the wave sensor is not explicitly defined, this can be done with eqn.(10) resulting in a frequency-dependent time-delay. In reality a radar scanner would be employed for this problem to scan a 2D or 3D wave field, compare, e.g. [22].

3.2. Impulse response fit

The causalized impulse response is subject to the system identification. For an identification in the time-domain the error of the original impulse response $\hat{\boldsymbol{y}}(t)$ compared to the simulated response $\boldsymbol{y}$ is minimized through an optimization of the model parameters and the initial conditions $\boldsymbol{x}_0$. The model parameters are the parameters of a state-space system with m states, which has therefore m free parameters in canonical form. The input dynamics are modeled through the parameters of the $\boldsymbol{B}$-matrix. Usually a nonlinear least-squares algorithm is used. Following the notation of [1] the cost function takes the form

$$\boldsymbol{Q} = \sum_{k=1}^{n} \boldsymbol{G}(t_k) \left[\hat{\boldsymbol{y}}(t_k) - \boldsymbol{C} e^{\boldsymbol{A} t_k} \boldsymbol{B} \right] \tag{12}$$

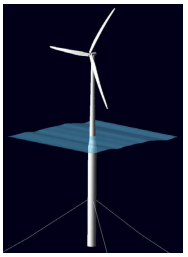

(a) OC3-Hywind spar [3].

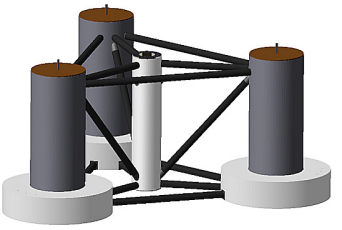

(b) OC4-DeepCwind semi-submersible, [F. Amann, SWE].

Fig. 3: Example FOWT platform geometries.

with the time-dependent weight matrix $\boldsymbol{G}(t)$ and input and output vectors $\boldsymbol{B}$ and $\boldsymbol{C}$, respectively. The initial conditions are here zero but the input is an impulse, which can be realized setting $\boldsymbol{x}_0 = \boldsymbol{B}$. Specific methods exist for the initialization of the parameters, for which the reader is referred to [21]. In this work the prediction-error minimization method of Matlab's system identification toolbox, see [23], is used with the Instrumental Variable (IV) method for pre-filtering with default settings. The discrete-to-continuous time signal conversion assumes a zero-order-hold (zoh) as inter-sample behavior. A review of state-of-the-art system identification techniques and a comparison of Matlab's system identification toolbox [23] with the CONTSID toolbox by the University of Lorraine can be found in [24]. Another possible method is the state-space realization of an impulse response using Hankel singular value decomposition (Matlab's `imp2ss` command). The latter method has been applied by [10] for a fit of the radiation impulse response function. The model structure is selected such that the infinite frequency limit of the identified transfer function $G_i(j\omega)$ is zero, $\lim_{\omega\to\infty} G_i(j\omega) = 0$. Therefore the relative degree is $r \geq 1$ and the transfer function $G_i(j\omega)$ is strictly proper. A nonzero steady-state amplification is not a problem here. A relatively small number of states (or poles) around $n = 6$ has given reasonable results for the studied geometries. As examples the OC3-Hywind spar, [3] and the OC4-DeepCwind semi-submersible, [4] have been selected. Their geometries are shown in Fig. 3 and the basic dimensions collected in Table 1.

Table 1: FOWT platform model dimensions.

		OC3-Hywind spar	OC4-DeepCwind semi-submersible
Mass including ballast	[t]	7,466	13,473
Volume of displaced water	[m^3]	$0.803 \cdot 10^4$	$1.39 \cdot 10^4$
Draft	[m]	120.0	20.0
Breadth	[m]	9.4	74.0

3.2.1. OC3 spar

For the OC3 spar the panel code Wamit, [25], has been used with a constant frequency resolution of $\Delta f = 0.008$ Hz up to a frequency of $f = 0.8$ Hz. The results are taken from [4]. The impulse response of the wave excitation transfer function $\boldsymbol{G}_{frc}$ has been shifted in time for causalization as explained in section 3.1 with a time delay $\tau_c = 6$ s. In order to study the necessary number of states for the model fit the panel code wave excitation transfer function as magnitude and phase components as well as the impulse response through an inverse Fourier transform as eqn. (8) has been plotted together with models of $n = [4, 6, 8]$ states in Fig. 4. The agreement of the model fit in terms of percent fit and Mean-Squared Error (MSE) can be found in Tab. 2. The 4-state model has clear deviations visible in the transfer function but also in the impulse response, especially in surge. The 6- and 8-state model on the other side converge better to the target model of the panel code. A model with $n = 6$ states and an agreement to the original model of 87.9 % has been chosen for all remaining calculations in this paper. The model has input dynamics with an order of 5 and consequently the transfer function $\boldsymbol{G}_{frc}$ has a relative degree $r = 1$ for all directions i.

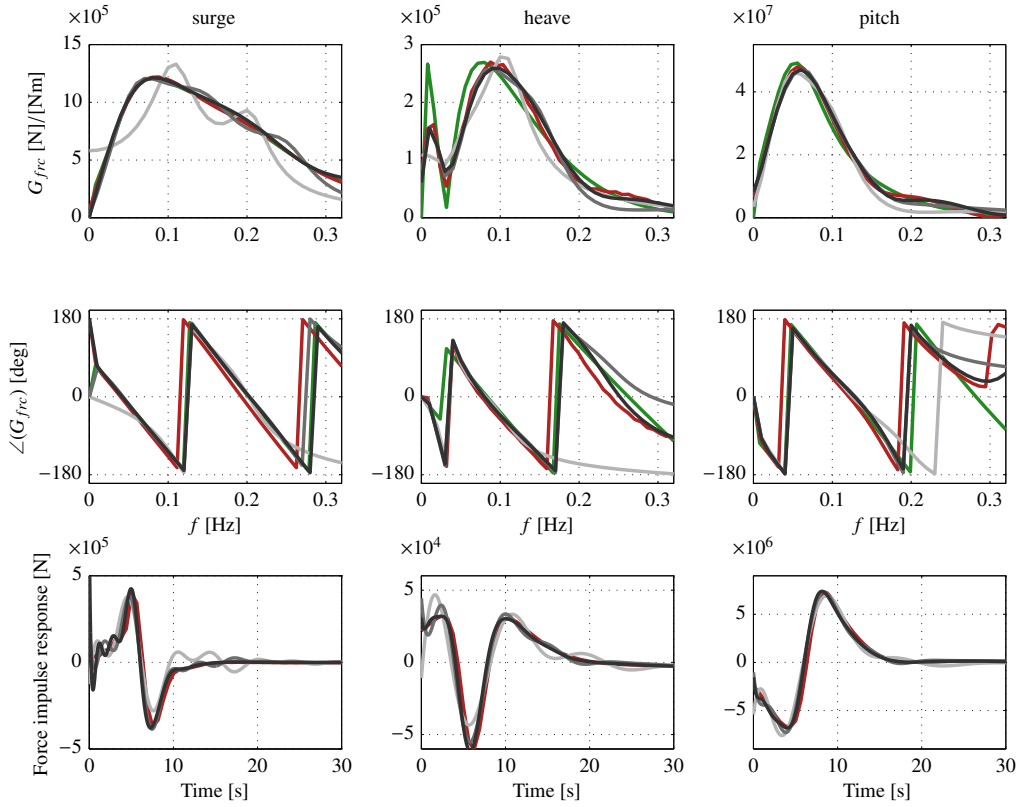

Fig. 4: Panel code (green), causalized (red), model fit with $n_{states} = [4, 6, 8]$ (grey, increasing darkness), OC3 spar.

Figure 5 shows the response of the fitted model to irregular waves with a comparison to the inverse Fourier transform of eqn. (8). The wavetrain used is of the Jonswap spectrum with peak periods of $T_p = [5, 10, 15]$ s and a significant wave height $H_s = 3$ m. The fitted model for the OC3 spar is the one with $n = 6$ states and a time delay $\tau_c = 6$ s. The surge and pitch responses show a very good agreement, also for high-frequency waves of $T_p = 5$ s on top of Fig. 5. For the heave responses, especially for $T_p = 15$ s some small differences to the original data is visible.

3.2.2. OC4 semi-submersible

For the more complex hull shape of the OC4 semi-submersible the same comparison has been made with the transfer function and the impulse response for the panel code result and the fitted model. The panel code transfer function shows for this three-column semi-submersible more peaks than the one of the spar-type OC3 platform. The panel code calculations have been performed by [4] with a frequency resolution of $df = 0.0016$ Hz up to a frequency of $f_{max} = 0.79Hz$. The hydrodynamic forces of this semi-submersible differ from the previously described cylindric shape. Therefore, viscous effects, among others, might be of importance. They are only represented in the model used here by linear damping coefficients, defined in [4]. For the model fit the impulse response function has been shifted in time with a time delay of $\tau_c = 7.5$ s. The quality of the model fit is shown in Fig. 6. Again, with the transfer function and impulse response for $n = [4, 6, 8]$ states. It was to be expected that for this more complex hull $n = 4$ states would, as for the OC3 spar, not suffice. But as in the case of the OC3 spar the models with four and six states show a good agreement in both, the frequency and time response. Thus, also for the OC4 semi-submersible a model of $n = 6$ states has been chosen for the remainder of the paper. This model has input dynamics with an order of 5

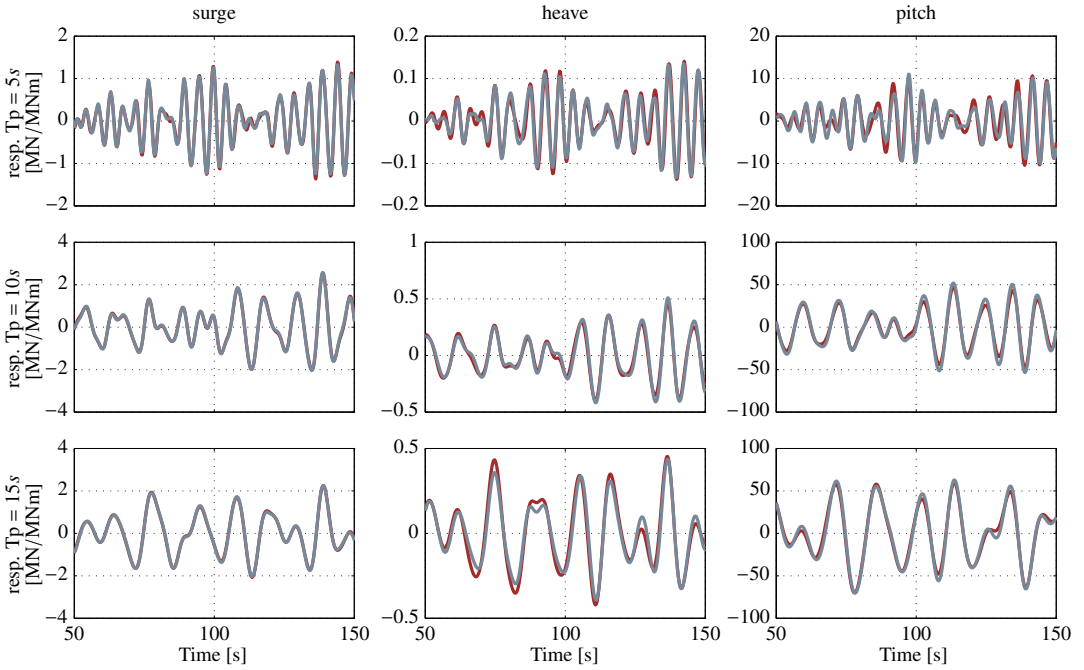

Fig. 5: Wave force response by inverse Fourier transform (red) and 6-state fitted model (grey) for $T_p = [5, 10, 15]$s, OC3 spar.

Table 2: Panel code and fitted model data of OC3 and OC4 platforms.

		OC3-Hywind spar	OC4-DeepCwind semi-submersible
Panel code freq. resolution df	[Hz]	0.008	0.0016
Panel code max. frequency f_{max}	[Hz]	0.79	0.79
Model fit time delay τ_c	[m]	6.0	7.5
4-state model	[−]		
Model fit	[%]	81.2	64.0
Mean Square Error (MSE)	[−]	$9.5 \cdot 10^{10}$	$1.8 \cdot 10^{11}$
6-state model	[−]		
Model fit	[%]	87.9	74.9
Mean Square Error (MSE)	[−]	$4.0 \cdot 10^{10}$	$9.0 \cdot 10^{10}$
8-state model	[−]		
Model fit	[%]	89.5	76.2
Mean Square Error (MSE)	[−]	$3.0 \cdot 10^{10}$	$8.0 \cdot 10^{10}$

and so the transfer function $\boldsymbol{G}_{frc}$ also has a relative degree $r = 1$. Figure 7 shows the response of the fitted model to irregular waves with a comparison to the inverse Fourier transform as above for the OC3 spar. Especially for the high-frequency waves on top of Fig. 7, the identified model does not capture all characteristics. For the longer waves of $T_p = 10, 15$ s the surge and pitch responses show a better agreement than the heave response. This might be due to the shape of the phase response of the causalized model, which is not captured for all frequencies $f < 0.1$ Hz.

The OC3-Hywind floating wind turbine model is, in terms of geometry, quite close to the one studied by [1]. However, floating wind turbine foundations have often more complex hull shapes, like for example, the OC4-DeepCwind semi-submersible. The results show that a very good fit is possible for the OC3-Hywind shape but surprisingly a

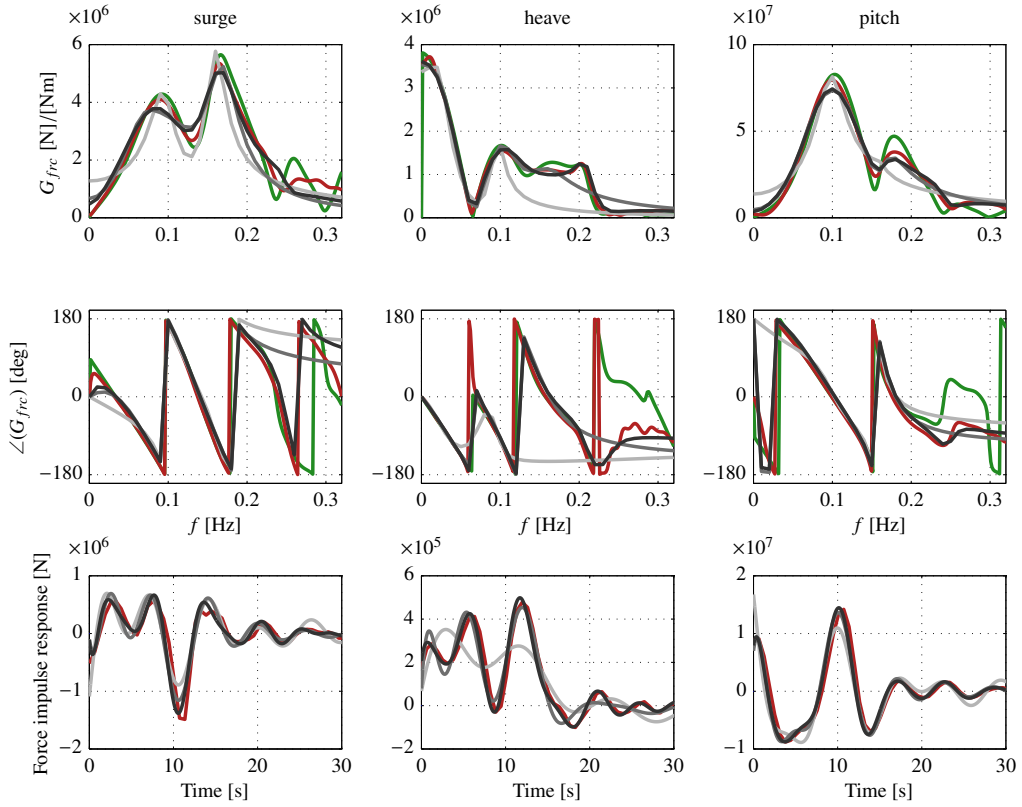

Fig. 6: Panel code (green), causalized (red), model fit with $n_{states} = [4, 6, 8]$ (grey, increasing darkness), OC4 semi-submersible.

fit with only 6 states for the shape of the OC4-semi-submersible gives an approximation that is considered accurate enough for the purpose of representing the overall system dynamics. Table 3 shows the numeric transfer function values for the two geometries. The next section will address the coupled FOWT system as flexible multi-body (FMBS) model in order to assess the disturbance transfer function from wave height to the states of the FOWT model.

Table 3: 6-state transfer functions and delay time τ_c for OC3 and OC4 platforms, wave propagation is aligned with x.

	Dir	τ_c	Numerator coefficient						Denominator coefficient						
		[s]	s^5	s^4	s^3	s^2	s^1	s^0	s^6	s^5	s^4	s^3	s^2	s^1	s^0
OC3	1	6.0	$2.4 \cdot 10^5$	$-6.5 \cdot 10^5$	$1.8 \cdot 10^6$	$-1.7 \cdot 10^6$	$1.4 \cdot 10^6$	$9.2 \cdot 10^3$	1.0	1.6	4.7	4.4	4.4	1.7	0.4
	3	6.0	$1.1 \cdot 10^4$	$9.0 \cdot 10^4$	$-2.8 \cdot 10^4$	$2.2 \cdot 10^5$	$-2.9 \cdot 10^4$	$9.6 \cdot 10^3$	1.0	1.6	3.2	2.5	1.7	0.4	0.08
	5	6.0	$-4.3 \cdot 10^6$	$-1.7 \cdot 10^6$	$-3.0 \cdot 10^7$	$5.9 \cdot 10^6$	$-3.3 \cdot 10^7$	$8.9 \cdot 10^5$	1.0	2.4	4.2	4.4	2.8	1.0	0.2
OC4	1	7.5	$-1.0 \cdot 10^5$	$-1.0 \cdot 10^6$	$1.1 \cdot 10^6$	$-8.7 \cdot 10^5$	$5.3 \cdot 10^5$	$9.0 \cdot 10^4$	1.0	1.0	2.3	1.4	1.3	0.4	0.1
	3	7.5	$7.9 \cdot 10^4$	$7.4 \cdot 10^5$	$-1.8 \cdot 10^5$	$7.1 \cdot 10^5$	$-3.3 \cdot 10^4$	$9.9 \cdot 10^4$	1.0	1.0	1.8	1.0	0.7	0.2	0.03
	5	7.5	$7.0 \cdot 10^6$	$1.8 \cdot 10^7$	$-2.1 \cdot 10^5$	$1.9 \cdot 10^7$	$-4.1 \cdot 10^6$	$-7.4 \cdot 10^5$	1.0	1.1	2.3	1.6	1.4	0.4	0.2

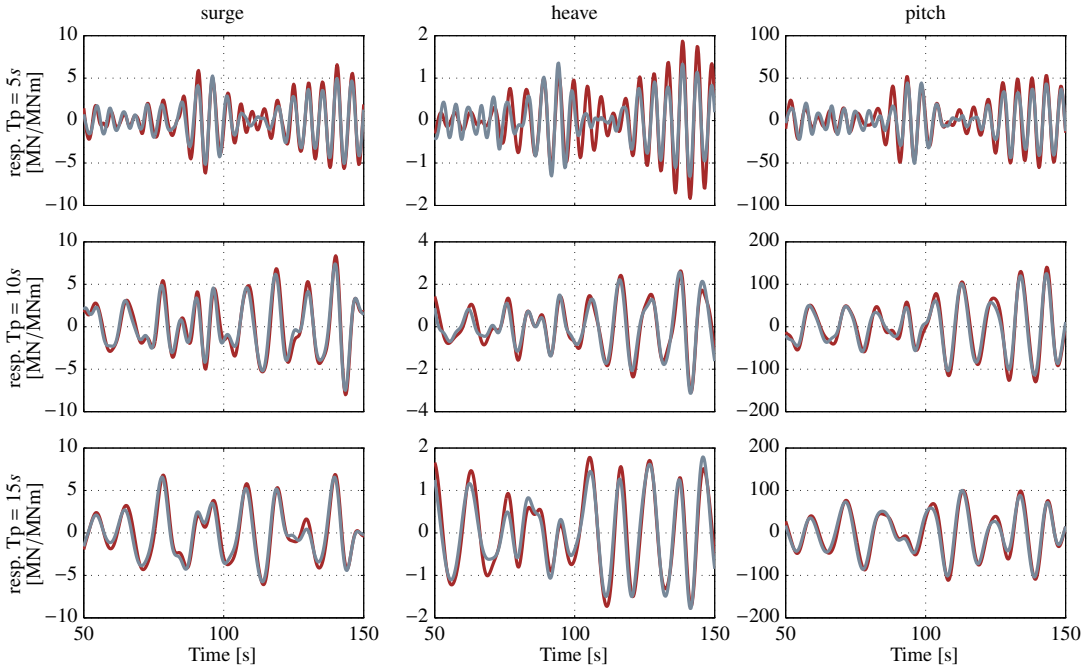

Fig. 7: Wave force response by inverse Fourier transform (red) and 6-state fitted model (grey) for $T_p = [5, 10, 15]$s, OC4 semi-submersible.

4. Structural floating wind turbine model

The coupled FOWT is a multi-disciplinary system of various components, each one having its own dynamics, see Fig. 1. The usual modeling approach is a flexible multibody model with modal shape functions for the flexible bodies of tower and blades. Hydrodynamics are usually modeled through Cummins equation as described in Section 2.1 and aerodynamics are commonly modeled through the iterative solution of the Blade-Element Momentum Theory (BEM). State-of-the-art tools are the open-source FAST code by NREL or the commercial software HAWC2 by DTU and Bladed by DNVGL. Here, a somewhat different approach is chosen: A simplified model, developed at the University of Stuttgart, integrated in Matlab/Simulink with a modular structure and symbolic equations of motion is used. The work on the model started in 2012 with the objective of standalone symbolic equations (the whole right-hand side of the ordinary differential equation is not set up step by step as numeric values but is available in the program code directly in terms of symbolic variables). This has first the advantage of computational speed but it is also straightforward to implement the equations in other environments like real-time systems for model-based control. The nonlinear symbolic equations can be linearized for linear system analysis. The tool started with Newton-Euler equations for rigid bodies linked by spring-damper elements and Morison Equation for hydrodynamics, quasi-static mooring lines and "actuator-point aerodynamics", see [26]. It has now been extended for flexible bodies and is coupled to the AeroDyn-BEM model by NREL. It has been applied for fast design load calculations [27], as internal model for linear and nonlinear model-predictive control [17], [18] and for controller design of floating wind turbines in [28]. The latter is an important driver for the present work: With the wave excitation "disturbance" transfer function the dynamics from the input wave height to the system output, like e.g. tower bending is known and can be incorporated the design of the controller for optimal disturbance attenuation.

The model is shortly introduced for the reader to understand the basic assumptions in the next sections before the linear disturbance dynamics are verified with the nonlinear model.

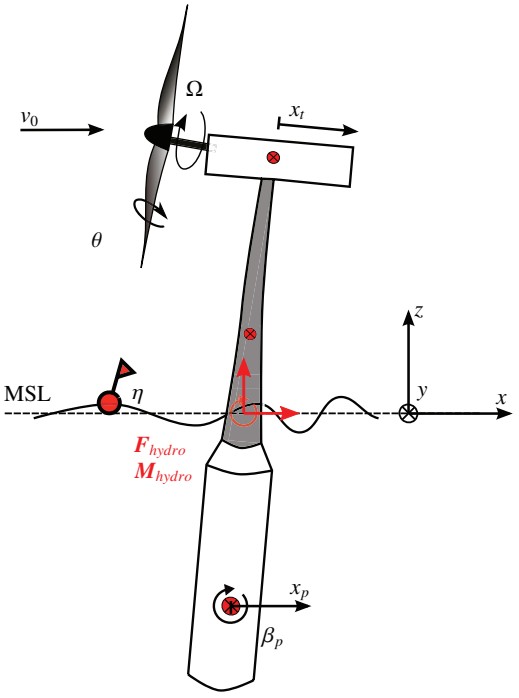

Fig. 8: Topology of the simplified multibody model.

4.1. Flexible multibody system description

A multibody model is based on the assumption of a large rigid-body reference motion together with small elastic deformations. If no flexible bodies are involved the rigid-body system consists of point-mass bodies coupled with spring-damper elements. Newton's second law for translational motion and Euler's law for rotational motion is set up for each of the different bodies i and thus, no conservation of energy is applied as in Lagrange's principle, but the momentum equations are set up directly. Forces $\boldsymbol{f}_i$ and moments $\boldsymbol{l}_i$ acting on the bodies can be defined as state-dependent or time-dependent applied forces, where the latter result from a system input.

An input file for setting up the equations of motion includes the position vector $\boldsymbol{r}_i(\boldsymbol{q})$ to the center of mass of each body in inertial coordinates and the angular velocity vector $\boldsymbol{\omega}_i(\boldsymbol{q})$ based on the generalized coordinates $\boldsymbol{q}$. Also the point mass properties as mass m_i and inertia tensor $\boldsymbol{I}_i$ are necessary. In this work the equations of motion have been set up for four DOFs in 2D: Three rigid DOFs as platform surge x_p, platform pitch β_p and rotor azimuth φ combined in $\boldsymbol{q}_r$ and the elastic tower fore-aft deformation x_t in $\boldsymbol{q}_e$

$$\boldsymbol{q} = \begin{bmatrix} x_p \\ \beta_p \\ \varphi \\ x_t \end{bmatrix}, \qquad \boldsymbol{q}_r = \begin{bmatrix} x_p \\ \beta_p \\ \varphi \end{bmatrix}, \qquad \boldsymbol{q}_e = \begin{bmatrix} x_t \end{bmatrix}. \tag{13}$$

The rigid bodies are the *platform*, *nacelle* and the *rotor* and the only elastic body is the *tower*, see Fig. 8. The tower shape function used is the first fore-aft mode shape. The wind turbine is the NREL 5 MW wind turbine, of which the properties can be found in [2]. The individual rotor blades are not included in this model but the rotor is modeled as a rigid disk. This method neglects the coupling of edgewise blade dynamics with the tower modes. It is still used here because it simplifies the model to a significant extent and allows a clearer view on the main system dynamics. With

this the translational and angular velocity and acceleration of each body's center of mass in inertial coordinates can be calculated by the kinematic equations. Here, the kinematics are set up based on Jacobi matrices, following [29]

$$\boldsymbol{J}_{Ti} = \frac{\partial \boldsymbol{r}_i}{\partial \boldsymbol{q}} \qquad\qquad \boldsymbol{J}_{Ri} = \frac{\partial \boldsymbol{\omega}_i}{\dot{\boldsymbol{q}}}. \tag{14}$$

This is advantageous for a numerical setup of the kinematics function. The velocity and angular velocity vectors remain for each body i as

$$\boldsymbol{v}_i = \boldsymbol{J}_{Ti}\dot{\boldsymbol{q}} \qquad\qquad \boldsymbol{\omega}_i = \boldsymbol{J}_{Ri}(\boldsymbol{q}) \cdot \dot{\boldsymbol{q}}, \tag{15}$$

if no time-dependent boundary conditions exist (scleronomic system). Accordingly, the translational and rotational accelerations of body i are

$$\boldsymbol{a}_i = \dot{\boldsymbol{v}}_i = \boldsymbol{J}_{Ti} \cdot \ddot{\boldsymbol{q}} + \dot{\boldsymbol{J}}_{Ti} \cdot \dot{\boldsymbol{q}} \qquad\qquad \boldsymbol{\alpha}_i = \dot{\boldsymbol{\omega}}_i = \boldsymbol{J}_{Ri} \cdot \ddot{\boldsymbol{q}} + \dot{\boldsymbol{J}}_{Ri} \cdot \dot{\boldsymbol{q}}. \tag{16}$$

The Newton-Euler equations with three rows for Newton's law and three rows for Euler's law for each body i remain as

$$\begin{bmatrix} m_i \boldsymbol{E} \cdot \boldsymbol{J}_{Ti} \\ \vdots \\ \boldsymbol{I}_i \cdot \boldsymbol{J}_{Ri} \\ \vdots \end{bmatrix} \ddot{\boldsymbol{q}} + \begin{bmatrix} m_i \boldsymbol{E} \dot{\boldsymbol{J}}_{Ti} \cdot \dot{\boldsymbol{q}} \\ \vdots \\ \boldsymbol{I}_i \dot{\boldsymbol{J}}_{Ri} \cdot \dot{\boldsymbol{q}} \; + \; \tilde{\boldsymbol{\omega}}_i \boldsymbol{I}_i \boldsymbol{\omega}_i \\ \vdots \end{bmatrix} = \begin{bmatrix} \boldsymbol{f}_i \\ \vdots \\ \boldsymbol{l}_i \\ \vdots \end{bmatrix} + \overline{\boldsymbol{F}}_c. \tag{17}$$

Although the Newton-Euler equations are written for each body in all six directions the motion is usually constrained. The unknown reaction forces $\overline{\boldsymbol{F}}_c$ are the forces pointing into these constrained directions. These forces are not necessary for the calculation of the motion response and will be eliminated later.

Now the difference to elastic bodies compared to rigid bodies will be elaborated. Since the derivation of the equations for 3D kinematics and kinetics is rather complex an overview will be given with a reference to the respective literature. Here, the "floating frame of reference" method is followed, see [30]: A reference coordinate system for the flexible body is chosen, which is not necessarily its center of mass but any reference point that is convenient for the description of the elastic properties. The coordinate system used in the floating frame of reference formulation is the inertial one in [31] but here, the moving, body-fixed coordinate system is selected, as in [32]. This formulation simplifies parts of the equations and is useful for a pre-computation of the elastic properties of the bodies. Eventually, the kinematics of an elastic body i can be described by the reference kinematics and the generalized elastic coordinates $\boldsymbol{q}_{e,i}$. Thus, the translational and angular velocity and the acceleration of an elastic body i under the notation adopted from [33] is given by

$$z_{II,i} = \begin{bmatrix} {}^R\boldsymbol{v}_i \\ {}^R\boldsymbol{\omega}_i \\ \dot{\boldsymbol{q}}_{e,i} \end{bmatrix} = \begin{bmatrix} \boldsymbol{J}_{T,i}(\boldsymbol{q}) \\ \boldsymbol{J}_{R,i}(\boldsymbol{q}) \\ \boldsymbol{J}_{E,i} \end{bmatrix} \dot{\boldsymbol{q}} \qquad \text{and} \qquad z_{III,i} = \begin{bmatrix} {}^R\boldsymbol{a}_i \\ {}^R\boldsymbol{\alpha}_i \\ \ddot{\boldsymbol{q}}_{e,i} \end{bmatrix} = \begin{bmatrix} \boldsymbol{J}_{T,i}(\boldsymbol{q}) \\ \boldsymbol{J}_{R,i}(\boldsymbol{q}) \\ \boldsymbol{J}_{E,i} \end{bmatrix} \ddot{\boldsymbol{q}} + \begin{bmatrix} \dot{\boldsymbol{J}}_{T,i}(\dot{\boldsymbol{q}}) \\ \dot{\boldsymbol{J}}_{R,i}(\dot{\boldsymbol{q}}) \\ \boldsymbol{0} \end{bmatrix} \dot{\boldsymbol{q}}. \tag{18}$$

Consequently, the kinematics of elastic bodies are described by a reference translational and rotational motion as for rigid bodies, see eqn. (15) but additionally with the generalized coordinates of the elastic motion. Note that in the case of elastic bodies the reference coordinates are written in the local coordinate system denoted by the superscript R. The selection matrix $\boldsymbol{J}_{E,i}$ assigns the elastic coordinates $\boldsymbol{q}_{e,i}$ of $\boldsymbol{q}$ to the corresponding bodies. With these kinematics the Newton-Euler equations for elastic bodies can be set up as in the case of rigid bodies, eqn. (17). The kinetics of elastic bodies include further the quadratic velocity vector $\boldsymbol{h}_{\omega,i}$ with Coriolis, centrifugal and gyroscopic forces, the inner elastic forces $\boldsymbol{h}_{e,i}$, based on the selected deformation tensor, external and applied forces, including gravitational forces, $\boldsymbol{h}_a$ and again, the constraint forces $\boldsymbol{h}_c$. These are summed up together with the inertia forces from the mass matrix $\overline{\overline{\boldsymbol{M}}}_i$ resulting in the translational and rotational momentum equation

$$\overline{\overline{\boldsymbol{M}}}_i \begin{bmatrix} {}^R\boldsymbol{a}_i \\ {}^R\boldsymbol{\alpha}_i \\ \ddot{\boldsymbol{q}}_{e,i} \end{bmatrix} + \boldsymbol{h}_{\omega,i} + \boldsymbol{h}_{e,i} - \boldsymbol{h}_{a,i} + \boldsymbol{h}_{c,i} = \boldsymbol{0}. \tag{19}$$

The details of these equations can be found in [32] or in [31].

The global Newton-Euler equations of each, rigid and elastic, body are now transformed into "minimal coordinates" with each row representing one degree of freedom. Here, the unknown reaction forces have been eliminated using d'Alembert's principle: A transformation of eqn. (19) with the global Jacobian matrix $\overline{\boldsymbol{J}}$, the assembly of the translational and rotational Jacobi matrices of all bodies yields the nonlinear equations of motion in minimal coordinates. These can be transformed directly into state space

$$\dot{\boldsymbol{x}} = \frac{\partial \boldsymbol{x}}{\partial t} = \begin{bmatrix} \dot{\boldsymbol{q}} \\ \ddot{\boldsymbol{q}} \end{bmatrix} = \begin{bmatrix} \dot{\boldsymbol{x}} \\ \boldsymbol{M}^{-1}(\boldsymbol{p}(\boldsymbol{q}, \dot{\boldsymbol{q}}) - \boldsymbol{k}(\boldsymbol{q}, \dot{\boldsymbol{q}})) \end{bmatrix}, \tag{20}$$

where the input forces on the platform, the mooring forces and wave excitation forces $\boldsymbol{F}_{hydro} = \boldsymbol{F}_{moor} + \boldsymbol{F}_{wave}$, are part of vector $\boldsymbol{p}$.

4.2. Mooring line model

The mooring lines are the ones described in the OC3 and OC4 definition papers [3] and [4]. A quasi-static mooring model has been used to obtain the force-displacement relationships for one line. The resulting overall forces on the *platform* body $\boldsymbol{F}_{moor}$ as functions of the mooring line kinematics are calculated in each timestep.

4.3. Linearized equations of motion

With the wave excitation force transfer function of Section 3 we want to calculate the linear transfer function from wave height η to the FOWT structural states. For this end the nonlinear equations of motion are linearized around the set point of the states $\boldsymbol{x}_0$ and the disturbance inputs $\boldsymbol{u}$

$$\boldsymbol{x} = \boldsymbol{x}_0 + \Delta\boldsymbol{x} \qquad\qquad \boldsymbol{u} = \boldsymbol{u}_0 + \Delta\boldsymbol{u}. \tag{21}$$

where $\Delta\boldsymbol{x}$ and $\Delta\boldsymbol{u}$ are the new vector of differential states and inputs, respectively. Ensuing the linearization the coupled equations of motion in state space description from equation (20) can be separated for position- and velocity-dependent terms. It remains with the input ($\boldsymbol{B}\Delta u$)

$$\Delta\dot{\boldsymbol{x}} = \underbrace{\begin{bmatrix} \boldsymbol{0} & \boldsymbol{E} \\ -\boldsymbol{M}^{-1}\boldsymbol{Q} & -\boldsymbol{M}^{-1}\boldsymbol{P} \end{bmatrix}}_{\boldsymbol{A}} \Delta\boldsymbol{x} + \boldsymbol{B}\Delta u. \tag{22}$$

One can identify the position-dependent matrix $\boldsymbol{Q}$ and the velocity-dependent matrix $\boldsymbol{P}$, which result from the transformation of the vector of Corliolis, centrifugal and gyroscopic forces and the applied forces. The linearization is especially critical for the aerodynamic force coefficients due to the high nonlinearity.

4.4. Disturbance transfer functions

With the linearized FOWT model the disturbance transfer function from wave height to any output of the FOWT system can now be calculated, see Fig. 1. For a verification of the fitted wave excitation transfer function $\boldsymbol{G}_{frc}$ and the structural transfer function from wave forces $\boldsymbol{F}_{wave}$ to the tower-top displacement x_t, eqn. (22), they have been compared to the nonlinear model of the OC4 semi-submersible: The nonlinear model, eqn. (20) has been run with regular unit-amplitude wave force timeseries as input, eqn. (8), until it reached a steady state. The amplitude and phase of the tower-top displacement x_t against the wave signal $\eta(t)$ was calculated by a Fourier transform of the timeseries for different wave frequencies. The OC4 semi-submersible has been simulated with an overall linear hydrodynamic damping coefficient of $\xi_{11} = 2\,\%$ and $\xi_{55} = 1\,\%$ and a constant added-mass coefficient of $A_{11,c} = 7.9 \cdot 10^6\,\mathrm{kg}$ and $A_{55,c} = 6.09 \cdot 10^9\,\mathrm{kgm}^2$. In order to focus on the wave model no aerodynamic forces act on the system. Figure 9 shows the comparison of the results of the linear model and the nonlinear model. Both, amplitude and phase fit very well and therefore the linear model is considered valid. It is mentioned that a higher-order viscous damping model

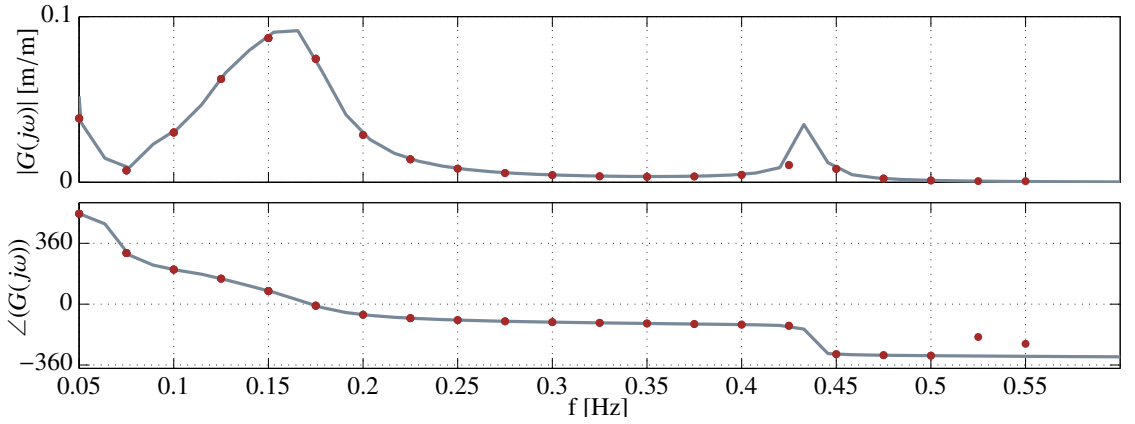

Fig. 9: Transfer function from wave height η to tower-top displacement x_t for OC4 semi-submersible. Linear model (grey), nonlinear model (red).

and a radiation model might alter the results of the linear and the nonlinear model. However, the simple narrow-band approach allows to better evaluate the difference coming from the fitted wave force model compared to the direct calculation of force timeseries.

5. Conclusions

An LTI model has been fitted to the linear wave excitation force coefficient from a panel code. The fitted model of two example platforms for FOWTs has been compared to the original panel code data in frequency and time-domain. The results show that with a little number of states it is possible to obtain a good agreement for realistic wave frequencies, even for a comlex semi-submersible shape in surge, heave and pitch direction. The wave excitation transfer function has been used to represent the disturbance dynamics of a coupled FOWT model and the overall transfer function from wave height to the wind turbine tower-top displacement has been calculated and verified through a comparison with the nonlinear FOWT model with the wave force timeseries as input. The fitted model is important for model-based controller design because the knowledge of the wave excitation dynamics can be used to design controllers for optimal disturbance rejection and load reduction.

Acknowledgements

The research leading to these results has received partial funding from both, the European Community's Seventh Framework Programme under grant agreement No. 308974 (INNWIND.EU) and the European Union's Horizon 2020 research and innovation programme under grant agreement No. 640741 (LIFES50+).

References

[1] Yu, Z., Falnes, J.. State-space modelling of a vertical cylinder in heave. Applied Ocean Research 1995;17(5):265–275. URL: http://www.marinecontrol.org/References/papers/YuFalnes1995.pdf. doi:10.1016/0141-1187(96)00002-8.

[2] Jonkman, J., Butterfield, S., Musial, W., Scott, G.. Definition of a 5-MW reference wind turbine for offshore system development. Tech. Rep. February; NREL; Boulder/USA; 2009. URL: http://www.nrel.gov/docs/fy09osti/38060.pdf.

[3] Jonkman, J.. Definition of the floating system for phase IV of OC3. Tech. Rep.; NREL; 2010.

[4] Robertson, A., Jonkman, J., Masciola, M., Song, H., Goupee, A., Coulling, A., et al. Definition of the semisubmersible floating system for phase II of OC4. Tech. Rep.; NREL; Boulder/USA; 2014. URL: http://www.nrel.gov/docs/fy14osti/60601.pdf.

[5] Newman, J.N.. Marine Hydrodynamics. MIT Press; 1977.

[6] Ogilvie, T.F.. Recent progress toward the understanding and prediction of ship motions. In: Proceedings of the Fifth Symposium on Naval Hydrodynamics. 1964,.

[7] Cummins, W.. The impulse response function and ship motion. Technical report 1661. Tech. Rep.; David Taylor Model BasinDTNSRDC; 1962.

[8] Jonkman, J.. Dynamics modeling and loads analysis of an offshore floating wind turbine. Ph.D. thesis; National Renewable Energy Laboratory; 2007.

[9] Yu, Z., Falnes, J.. State-space modeling of dynamic systems in ocean engineering. Journal of Hydrodynamics 1998;:1–17URL: http://166.111.121.20:9080/mathjournal/SDYW199801/sdyw199801000.caj.pdf.

[10] Pérez, T., Fossen, T.. Time-vs. frequency-domain identification of parametric radiation force models for marine structures at zero speed. Modeling, Identification and Control 2008;29(1):1–19. URL: http://marinecontrol.org/References/papers/MIC-2008-1-1.pdf. doi:10.4173/mic.2008.1.1.

[11] Kristiansen, E., Hjulstad, Å., Egeland, O.. State-space representation of radiation forces in time-domain vessel models. Modeling, Identification and Control 2006;27(1):23–41. doi:10.1016/j.oceaneng.2005.02.009.

[12] Pérez, T., Fossen, T.. A matlab toolbox for parametric identification of radiation-force models of ships and offshore structures. Journal of Modeling, Identification and Control 2009;30(1):1–15. URL: http://www.mic-journal.no/ABS/MIC-2009-1-1.asp. doi:10.4173/mic.2009.1.1.

[13] Jonkman, J., Buhl, M.. Fast user's guide. 2005.

[14] Duarte, T., Sarmento, A., Alves, M., Jonkman, J.. State-space realization of the wave-radiation force within Fast. 32nd International Conference on Ocean, Offshore and Arctic Engineering 2013;URL: http://www.nrel.gov/docs/fy13osti/58099.pdf. doi:10.1115/OMAE2013-10375.

[15] Sørensen, A., Sagatun, S., Fossen, T.. Design of a dynamic positioning system using model-based control. Control Engineering Practice 1996;4(3):359–368. doi:10.1016/0967-0661(96)00013-5.

[16] Lackner, M., Rotea, M.. Structural control of floating wind turbines. Mechatronics 2011;21(4):704–719. URL: http://linkinghub.elsevier.com/retrieve/pii/S0957415810002072. doi:10.1016/j.mechatronics.2010.11.007.

[17] Schlipf, D., Sandner, F., Raach, S., Matha, D., Cheng, P.W.. Nonlinear model predictive control of floating wind turbines. In: Proceedings of the Twenty-third International Conference on Offshore and Polar Engineering (ISOPE). 2013, p. 440–447. URL: (author version) http://elib.uni-stuttgart.de/opus/volltexte/2013/8516/pdf/13TPC_987Schlipf.pdf.

[18] Lemmer, F., Raach, S., Schlipf, D., Cheng, P.W.. Prospects of linear model predictive control on a 10MW floating wind turbine. In: Proceedings of the ASME 34th International Conference on Ocean, Offshore and Arctic Engineering. St. John's/Canada; 2015,URL: http://elib.uni-stuttgart.de/opus/volltexte/2015/9895/.

[19] Schlipf, D., Simley, E., Lemmer, F., Pao, L., Cheng, P.W.. Collective pitch feedforward control of floating wind turbines using lidar. In: Proceedings of the Twenty-fifth International Conference on Offshore and Polar Engineering (ISOPE). 2015,.

[20] Falnes, J.. On non-causal impulse response functions related to propagating water waves. Applied Ocean Research 1995;17(6):379–389. URL: http://linkinghub.elsevier.com/retrieve/pii/S0141118796000077. doi:10.1016/S0141-1187(96)00007-7.

[21] Ljung, L.. System identification - Theory for the user. Upper Saddle River, NJ [u.a.]: Prentice-Hall; 2009. ISBN 0-13-656695-2.

[22] Alford, L., Beck, R.F., Johnson, J.T., Lyzenga, D., Nwogu, O., Zundel, A.. A real-time system for forecasting extremewaves and vessel motions. In: Proceedings of the ASME 2015 34th International Conference on Ocean, Offshore and Arctic Engineering. Saint John's/Canada; 2015,.

[23] Ljung, L., Singh, R.. Version 8 of the matlab system identification toolbox. In: 16th IFAC Symposium on System Identification. Brussels, Belgium. ISBN 9783902823069; 2012, p. 1826–1832. doi:10.3182/20120711-3-BE-2027.00061.

[24] Garnier, H.. Direct continuous-time approaches to system identification. Overview and benefits for practical applications. European Journal of Control 2015;24:50–62. URL: http://linkinghub.elsevier.com/retrieve/pii/S0947358015000588. doi:10.1016/j.ejcon.2015.04.003.

[25] Wamit, . Wamit user manual version 7.0. Tech. Rep.; MIT; 2011. URL: http://www.wamit.com/manualupdate/V71_manual.pdf.

[26] Sandner, F., Schlipf, D., Matha, D., Seifried, R., Cheng, P.W.. Reduced nonlinear model of a spar-mounted floating wind turbine. In: Proceedings of the German Wind Energy Conference DEWEK. Bremen, Germany; 2012,URL: http://elib.uni-stuttgart.de/opus/volltexte/2013/8439/pdf/Sandner_ReducedModel_Dewek2012.pdf.

[27] Matha, D., Sandner, F., Schlipf, D.. Efficient critical design load case identification for floating offshore wind turbines with a reduced nonlinear model. Journal of Physics: Conference Series 2014;555. URL: http://stacks.iop.org/1742-6596/555/i=1/a=012069?key=crossref.2cf58ea90e06a51553c9c6441bd0248d. doi:10.1088/1742-6596/555/1/012069.

[28] Sandner, F., Schlipf, D., Matha, D., Cheng, P.W.. Integrated optimization of floating wind turbine systems. In: Proceedings of the ASME 33rd International Conference on Ocean, Offshore and Arctic Engineering OMAE; vol. 9B. San Francisco. ISBN 978-0-7918-4554-7; 2014,URL: (author version) http://elib.uni-stuttgart.de/opus/frontdoor.php?source_opus=9120. doi:10.1115/OMAE2014-24244.

[29] Schiehlen, W., Eberhard, P.. Technische Dynamik - Rechnergestützte Modellierung mechanischer Systeme im Maschinen- und Fahrzeugbau. Wiesbaden: Springer Vieweg; 2014. ISBN 978-3-658-06184-5.

[30] Schwertassek, R., Wallrapp, O., Shabana, A.A.. Flexible multibody simulation and choice of shape functions. Nonlinear Dynamics 1999;20(4):361–380. doi:10.1023/A:1008314826838.

[31] Shabana, A.A.. Dynamics of multibody systems. Cambridge: Cambridge University Press; 2005. ISBN 0-521-85011-8.

[32] Schwertassek, R., Wallrapp, O.. Dynamik flexibler Mehrkörpersysteme: Methoden der Mechanik zum rechnergestützten Entwurf und zur Analyse mechatronischer Systeme ; mit 25 Tabellen. Fundamentals and advances in the engineering sciences; Vieweg Friedr. + Sohn Ver; 1999. ISBN 9783528066291.

[33] Seifried, R.. Dynamics of underactuated multibody systems: modeling, control and optimal design. Cham; Heidelberg [u.a.]: Springer International Publishing; 2014. ISBN 978-3-319-01227-8. URL: http://swbplus.bsz-bw.de/bsz398366977cov.htm. doi:10.1007/978-3-319-01228-5.